published in Morskoy Gidrofizicheskiy Zhurnal, 2025, Vol. 41, Iss. 5, pp. 611-630

Original article

Statistical Characteristics of the Background Microseismic Field

G. I. Dolgikh ¹, S. G. Dolgikh ^{1, 2}, M. P. Ivanov ^{1, 2, ⊠}, E. N. Pelinovsky ^{3, 4, 5}, T. G. Talipova ³

¹ V. I. Il'ichev Pacific Oceanological Institute, Far Eastern Branch of Russian Academy of Sciences, Vladivostok, Russian Federation

² Institute of Automation and Control Processes, Far Eastern Branch of Russian Academy of Sciences, Vladivostok, Russian Federation

³ A. V. Gaponov-Grekhov Institute of Applied Physics, Russian Academy of Sciences, Nizhny Novgorod, Russian Federation

⁴ Higher School of Economics University, Nizhny Novgorod, Russian Federation
⁵ Nizhny Novgorod State Technical University n. a. R. E. Alekseev, Nizhny Novgorod, Russian Federation

■ Ivanov.mp@poi.dvo.ru

Abstract

Purpose. The purpose of this study is to investigate the statistical characteristics of the background microseismic field recorded by horizontal unequal-arm laser strainmeters and to assess deviations of the data from a normal distribution.

Methods and Results. The study involved data from two laser strainmeters developed using modern laser-interferometry techniques and installed at the Cape Shults Marine Experimental Station of POI FEB RAS (Primorsky Krai). The analysis focused on microdeformations of the Earth's crust upper layer measured by laser strainmeters with measuring arm lengths of 52.5 m (North – South orientation) and 17.5 m (West – East orientation). The microseismic noise field was statistically analyzed using data from these laser-interferometric devices for 2019–2020. The considered frequency range (0.05–0.5 Hz) includes microseisms generated by both terrestrial and marine processes (wind and swell waves). The statistical properties of the signals were comprehensively analyzed, including evaluation of skewness and kurtosis coefficients. Deviations from normal distribution were identified, and the Gram-Charlier series, which demonstrated the best correlation with empirical data, was applied to describe the probability density function. Kurtosis was predominantly positive for both components, indicating a high likelihood of large-amplitude outliers.

Conclusions. The performed analysis enabled quantitative assessment of background signal deviations from normal distribution and revealed their key statistical features. These results are crucial for analyzing microseismic background characteristics, as deviations from normality facilitate the study of physical mechanisms underlying the generation and interaction of oceanic, atmospheric and lithospheric processes.

Keywords: microseismic oscillations, laser strainmeter, noise characteristics, statistical characteristics, skewness coefficient, kurtosis coefficient, Fourier transform, Gram-Charlier series

Acknowledgments: The study was carried out with partial financial support from grant No. 075-15-2024-642 "Study of the processes and patterns of occurrence, development and transformation of catastrophic phenomena in the oceans and at the continents using seismoacoustic monitoring methods".

For citation: Dolgikh, G.I., Dolgikh, S.G., Ivanov, M.P., Pelinovsky, E.N. and Talipova, T.G., 2025. Statistical Characteristics of the Background Microseismic Field. *Physical Oceanography*, 32(5), pp. 624-642.

© 2025, G. I. Dolgikh, S. G. Dolgikh, M. P. Ivanov, E. N. Pelinovsky, T. G. Talipova

© 2025, Physical Oceanography

ISSN 1573-160X PHYSICAL OCEANOGRAPHY VOL. 32 ISS. 5 (2025)



624

Introduction

The study of the Earth's background field is essential for understanding the interactions within the atmosphere – hydrosphere – lithosphere system. Successful investigation of these interactions is impossible without experimental research in each geosphere and subsequent comparison of the obtained data. Recently, primary measuring instruments have included seismometers, microbarographs, wave recorders, wave radars, etc. Seismometers register ground displacement [1], microbarographs record atmospheric pressure variations [2], while wave recorders and wave radars measure various characteristics of sea waves [3, 4]. Comparing the obtained experimental data enables identification of new interaction patterns between the lithosphere, hydrosphere and atmosphere across various frequency ranges.

This study examines microseismic oscillations recorded by a specialized measuring complex installed on the coastal cliffs of the Sea of Japan at Shultz Cape, one of the research sites of the Pacific Oceanological Institute, Far Eastern Branch of the Russian Academy of Sciences [5]. For this purpose, high-precision equipment is used that can register, over a wide frequency range, not only microseisms caused by strong natural events – such as typhoons [6], earthquakes [7], and atmospheric fronts [8] – but also background oscillations induced, for example, by regular wind waves [9].

The study of background oscillations enables detection of microseismic activity with extremely low amplitudes and allows detailed analysis of the dynamic characteristics of the recorded microseismic signals.

The high-precision equipment consists of laser strainmeters based on modern laser interferometry methods [10]. This study utilizes data from two such laser strainmeters, described below. They are installed away from populated areas and traffic flows and record processes occurring at the land-water interface, taking into account atmospheric phenomena. This work is devoted to investigating the statistical characteristics of the background signal recorded by these strainmeters.

The frequency range of interest is 0.05–0.5 Hz (periods of 2–20 s), which corresponds to microseisms generated by sea waves (wind waves and swell). These oscillations are almost always present in the records because sea waves regularly break at the foot of the cliffs, thereby generating the corresponding microseisms. The specified frequency range is characterized by high energy density and is sensitive to changes in the hydrosphere [11, 12]. Furthermore, this range includes frequencies corresponding to atmospheric pressure variations (typhoons, storm fronts) and anthropogenic factors (movement of vehicles, ships, or people). These oscillations are irregular and not very intense, but they are nevertheless also present in the records.

Extraction of signals of interest is impossible without determining the noise characteristics of microseisms [13–15]. Recent research in this field has focused on analyzing frequency spectra and the amount of energy transferred from the ocean to the Earth's crust [16, 17]. At the same time, the statistical characteristics of the background noise (probability distributions and statistical moments) remain unstudied. These characteristics are extremely important for optimal extraction of useful signals, as they enable minimization of distortions and improvement of analysis accuracy.

The objective of this study is to investigate the statistical characteristics of the microseismic noise field recorded by two strainmeters and to assess the deviations of the data from a normal distribution. The investigation of the noise field is based on experimental data obtained with high accuracy under relatively calm weather conditions. For the first time, an analysis of skewness and kurtosis for the signals of two orthogonally oriented components has been conducted.

Measuring equipment

Field data were obtained using two laser strainmeters installed at the *Cape Shultz* Marine Experimental Station of the POI FEB RAS in the south of Primorsky Krai.

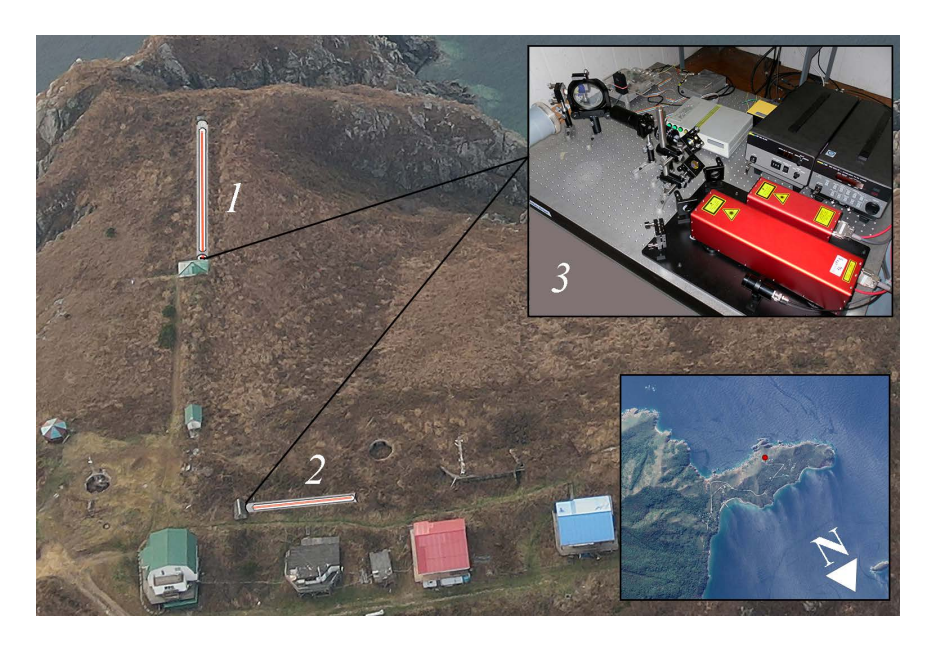


Fig. 1. Location of laser strainmeters. The North – South (I) and West – East (2) components, as well as the optical part of laser strainmeter (3) are shown

They are based on an unequal-arm Michelson interferometer [18] utilizing a frequency-stabilized helium-neon laser with long-term stability of 10^{-10} – 10^{-11} as the light source. This enables registration of microdeformation variations in the Earth's upper crust in the frequency range from 0 Hz (conventionally) to 10 kHz with an accuracy of 52.5 pm. The laser strainmeters are located on the coast of the Sea of Japan at an angle of 92° to each other (Fig. 1) in underground, thermally insulated rooms, oriented north-south and west-east, with measuring arm lengths of 52.5 m and 17.5 m, respectively. At any given time, both interferometers output two signal projections. The signals from the instruments, after preliminary processing, are formed into hourly files with a sampling frequency of 1000 Hz.

To select segments of instrument recordings with "maximum" background oscillations, data from a laser nanobarograph [19], a weather station, and a laser hydrosphere pressure variation meter [20] were used. Data where the amplitudes of

oscillations and waves in the frequency range of 0.05–0.5 Hz were minimal on the instrument recordings were selected. These data enable comprehensive analysis of seismic background fields in the coastal zone.

Table 1

Pe of Gram -Charlier (NS), Gauss 8.86 97.9 98.6 97.2 7.86 98.7 99.1 Ku(NS) 0.43 1.14 0.39 2.30 Processing data for the North - South component 0.047 0.004 0.068 0.097 0.118 0.060 0.055 0.112 0.025 0.007 0.091 0.051 σ(NS), μm 0.00013 0.00007 0.00013 0.00008 0.00024 0.00013 0.00044 0.00007 0.00025 0.00008 Average wind speed, Date of record 2.07.2019 2.07.2019 13.07.2019 4.07.2019 15.07.2019 17.07.2019 20.07.2019 24.07.2019 02.08.2019 07.08.2019 11.08.2019 07.06.2019 25.06.2019 2.07.2019 08.06.2020 9.09.2020 Start of record (1 hr), UTC 6:14:12 6:09:22 16:09:30 6:00:39 3:09:46 16:10:04 6:37:29 6:17:16 23:09:24 9:49:27 6:95:9 90:01:90 6:11:02 20:09:23 number File

rable 2

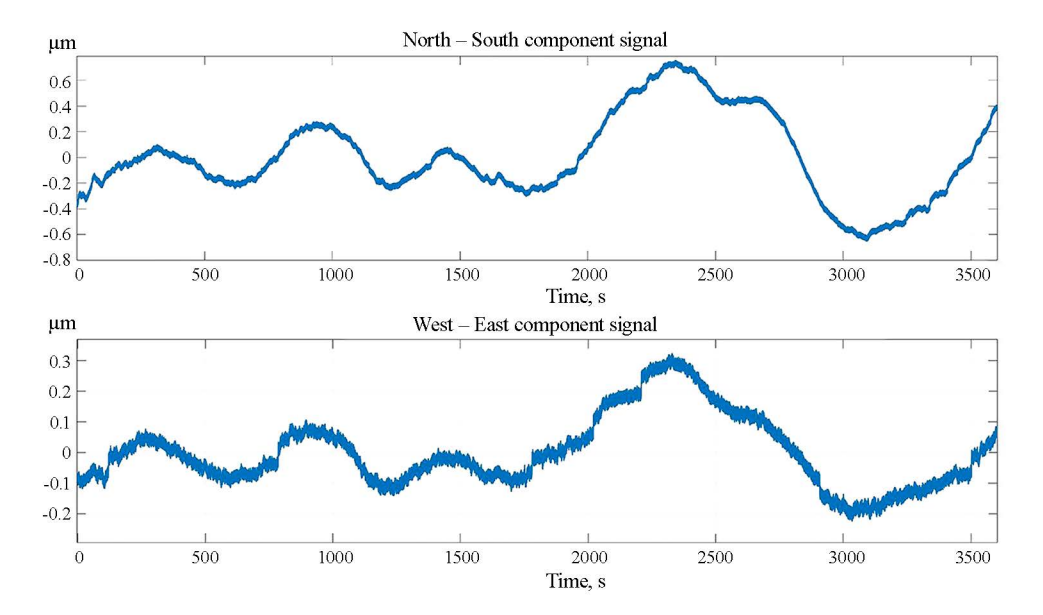
Processing data for the West - East component

		110003311	Hocessing data for the vest - East component	77 - 183 M	ndimon isi	IICIII		
- E-E	Chord of motor	Dotte of moon	Y	- WIE			Pe of	Pe of Gram –
rille	Start of record	Date of record	Average wind	o(WE),	Sk(WE)	Ku(WE)	Gauss	Charlier
Humber	(1 III), 01C	Start	speed, III/s	mm	Dec 2 Nov		(WE), %	(WE), %
	16:34:11	07.06.2019	1.7	0.00023	0.165	2.77	0.86	95.2
2	16:14:12	25.06.2019	8.4	0.00061	0.159	0.61	9.86	7.86
33	16:09:22	12.07.2019	1.1	0.00018	0.023	1.76	98.3	0.86
4	20:09:23	12.07.2019	1.7	0.00016	0.059	1.23	0.66	9.86
5	23:09:24	12.07.2019	4.4	0.00074	0.200	96:0	97.3	99.4
9	16:09:30	13.07.2019	5.1	0.00065	-0.250	4.76	82.5	92.7
7	16:09:39	14.07.2019	4.5	0.00035	0.051	0.33	0.66	99.1
8	13:09:46	15.07.2019	3.2	0.00126	-0.022	1.42	9.7.6	6.86
6	16:10:04	17.07.2019	7.1	0.00041	0.111	1.34	8.86	.66
10	16:37:29	20.07.2019	9.2	0.00317	-0.097	0.84	93.9	97.1
II	16:56:39	24.07.2019	2.4	0.00037	-0.017	2.79	97.3	96.1
12	06:10:06	02.08.2019	5.5	0.00124	-0.018	1.08	97.3	0.66
13	16:11:02	07.08.2019	8.5	0.00512	0.071	1.17	98.5	99.1
14	16:11:39	11.08.2019	4.6	0.00151	-0.318	1.56	2.96	6.86
15	16:17:16	08.06.2020	1.5	0.00022	-0.285	0.91	6.76	7.86
91	19:49:27	19.09.2020	4.5	0.00077	0.008	1.30	7.76	0.66

Data analysis

Sixteen 1-hour fragments of background recordings were selected for processing in both projections. These fragments were recorded during relatively calm weather without particularly strong outliers in 2019 and 2020.

The characteristics of the fragments are provided in Table 1, which specifies the date and start time of each recording. One sample of an hourly recording from the two interferometers is shown in Fig. 2. Good correlation between them is visible even to the naked eye. Some differences in the appearance of the signals are due to the different arm lengths of the interferometers.



 ${f Fig.~2}$. Example of an hour-long record of the signal received from two strainmeters. The vertical axis shows variations in microdeformations of the Earth's crust (μm)

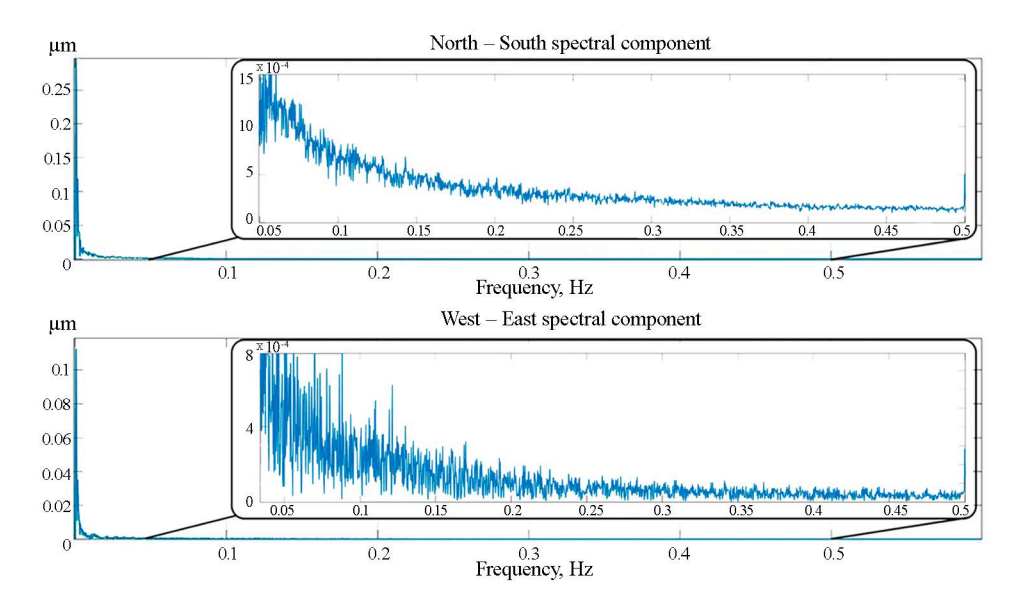
These data underwent preliminary processing using the MatLab software package. Fig. 3 shows the signal spectrum magnitude, obtained via the fast Fourier transform, which characterizes the distribution of spectral amplitudes:

$$X_k = \sum_{n=0}^{N-1} x_n \cdot e^{-i2\pi \frac{kn}{N}} \,, \tag{1}$$

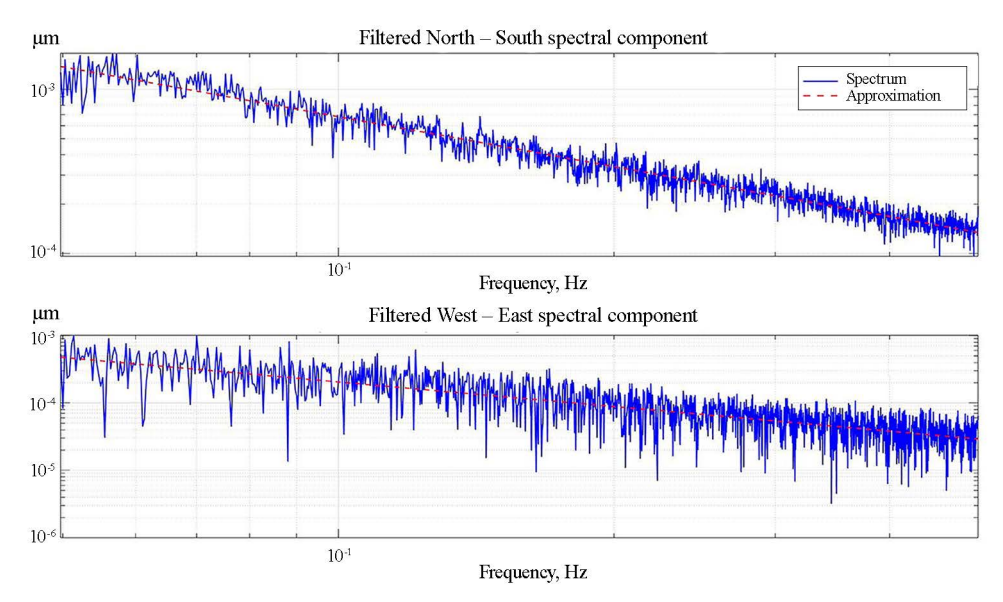
where N = 7200000.

The obtained signal spectra were used to analyze the frequency composition of the noise field. The Fourier transform allowed the signal to be decomposed into its constituent frequencies and the dominant ranges within them to be determined. A band-pass filter was applied to eliminate high-frequency noise and isolate microseisms, which are largely caused by wave impacts on the shore and sea bottom. The filter's passband was limited to the range of 0.05–0.5 Hz, corresponding to periods of 2–20 s, which are characteristic of wind waves, swell and microseisms. This made it possible to narrow the spectrum of analyzed frequencies to the target range, excluding unwanted high-frequency noise components and extracting the useful signal corresponding to the characteristic periods of microseisms. Furthermore, to visualize the frequency component, the signal spectrum after bandpass filtering was plotted on a double logarithmic scale (Fig. 4), and an analysis of

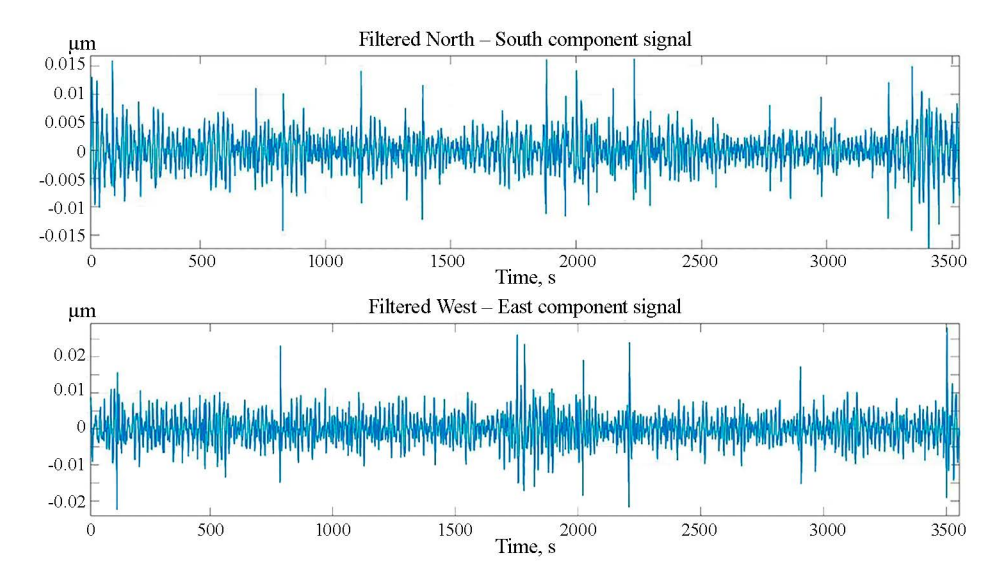
the spectral slope ω^{-p} was carried out. The approximation showed that for the North – South component, the exponent p was 1, while for the West – East component, p = 1.2. In the power spectrum, the exponent doubles, and p = 2-2.4 lies within the range of exponents for hydrodynamic turbulence (5/3) and shallow-water wind waves (3).



F i g. 3. Spectrum of the signal received from two strainmeters (tabs show the enlarged spectrum in the range 0.05-0.5 Hz). The vertical axis shows variations in microdeformations of the Earth's crust (μ m)



F i g. 4. Signal spectrum after filtration with a bandpass filter on a logarithmic scale in the frequency range 0.05-0.5 Hz. The vertical axis shows variations in microdeformations of the Earth's crust (μ m)



F i g. 5. Signal after filtration with a bandpass filter for two components of strainmeters. The vertical axis shows variations in microdeformations of the Earth's crust (μ m)

Subsequently, the signals from the two strainmeters were reconstructed after filtering (Fig. 5) using the inverse Fourier transform:

$$x_n = \frac{1}{N} \sum_{n=0}^{N-1} X_k \cdot e^{i2\pi \frac{kn}{N}} . {2}$$

The filtered signals possess a stable structure with a well-defined noise background. These data were processed using statistical methods. Primarily, the mean values and root mean square deviations were calculated for each fragment in both projections. Since the two strainmeters have different arm lengths, and the signal magnitude is proportional to the length (the distance traveled by the light), the signals were normalized to an effective length of one meter [21]. The first statistical moments were determined using the following standard formulas of mathematical statistics:

mean value

$$\bar{x} = \frac{1}{N} \sum_{i=1}^{N} x_i , \qquad (3)$$

rms deviation

$$\sigma = \sqrt{\frac{1}{N-1} \sum_{i=1}^{N} (x_i - \bar{x})^2} . \tag{4}$$

The third and fourth moments were also calculated: skewness coefficient

$$Sk = \frac{1}{N \cdot \sigma^3} \sum_{i=1}^{N} (x_i - \bar{x})^3,$$
 (5)

kurtosis coefficient

$$Ku = \frac{1}{N \cdot \sigma^4} \sum_{i=1}^{N} (x_i - \bar{x})^4 - 3.$$
 (6)

The probability density functions computed from the above data were compared with the Gaussian distribution:

$$f(x) = \frac{1}{\sigma\sqrt{2\pi}} e^{\left(-\frac{(x-\bar{x})^2}{2\sigma^2}\right)}.$$
 (7)

Figs. 6–11 present the calculated histograms compared with the Gaussian distribution. To assess deviations from the Gaussian curve, the Gram-Charlier series [22] was also plotted for comparison, which is typically used for relatively minor deviations from a normal process:

$$f_{GC}(z) = f(z) \left(1 + \frac{Sk}{6} (z^3 - 3z) + \frac{Ku}{24} (z^4 - 6z^2 + 3) \right),$$
 (8)

where $z = \frac{x - \bar{x}}{\sigma}$.

To assess the accuracy of these approximations, the sum of squared errors (SSE) [23] was used:

$$SSE = \sum_{i=1}^{N} \left(y_{\text{histogram}}(x_i) - y_{\text{model}}(x_i) \right)^2.$$
 (9)

Here $y_{\text{histogram}}$ (x_i) represents the probability density values derived from the experimental data. These values represent the probability density calculated from the normalized data and distributed over the intervals; $y_{\text{model}}(x_i)$ are the values predicted by the theoretical formula (Gaussian distribution or Gram-Charlier series) for each corresponding value. The sum of squared errors for the histogram frequencies takes the following form:

$$Total \, Variance = \sum_{i=1}^{N} (y_{\text{histogram}}(x_i) - \bar{y})^2. \tag{10}$$

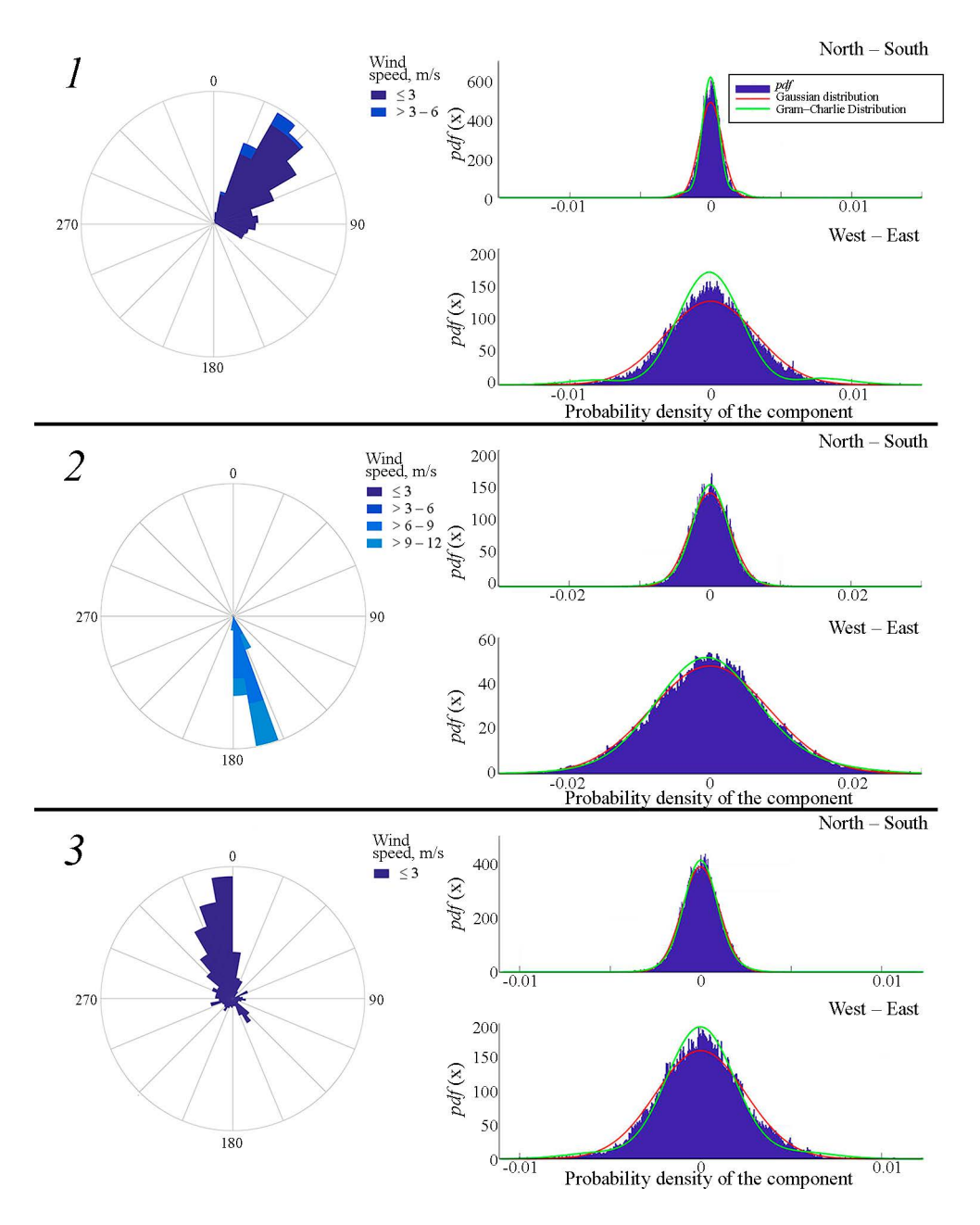
Using formulas (9) and (10), the percentage of explained variance Pe can be calculated:

$$Pe = \left(1 - \frac{SSE}{Total\ Variance}\right) \cdot 100. \tag{11}$$

Values of the average wind speed recorded during the operation of the two strainmeters were also taken into account. All these data are presented in Table 1 for the North – South component and in Table 2 for the West – East component.

Figs. 6–11 present the signal distribution histograms measured by the strainmeters oriented in the North – South and West – East directions (see

the fragments in Tables 1 and 2). The figures also show wind roses for the period of strainmeter recording. The histograms are shown as blue bars, the red curve represents the normal (Gaussian) distribution, and the green curve represents the Gram-Charlier distribution. Evidently, the Gram-Charlier distribution describes the actual distributions better than the Gaussian curve.



F i g. 6. Probability density of the normalized signal values from two strainmeters oriented in the north – south and west – east directions. I - 06.07.2019 during the time period from 16:34:11 to 17:34:11, 2 - 06.25.2019 – from 16:14:12 to 17:14:12, and 3 - 07.12.2019 – from 16:09:22 to 17:09:22

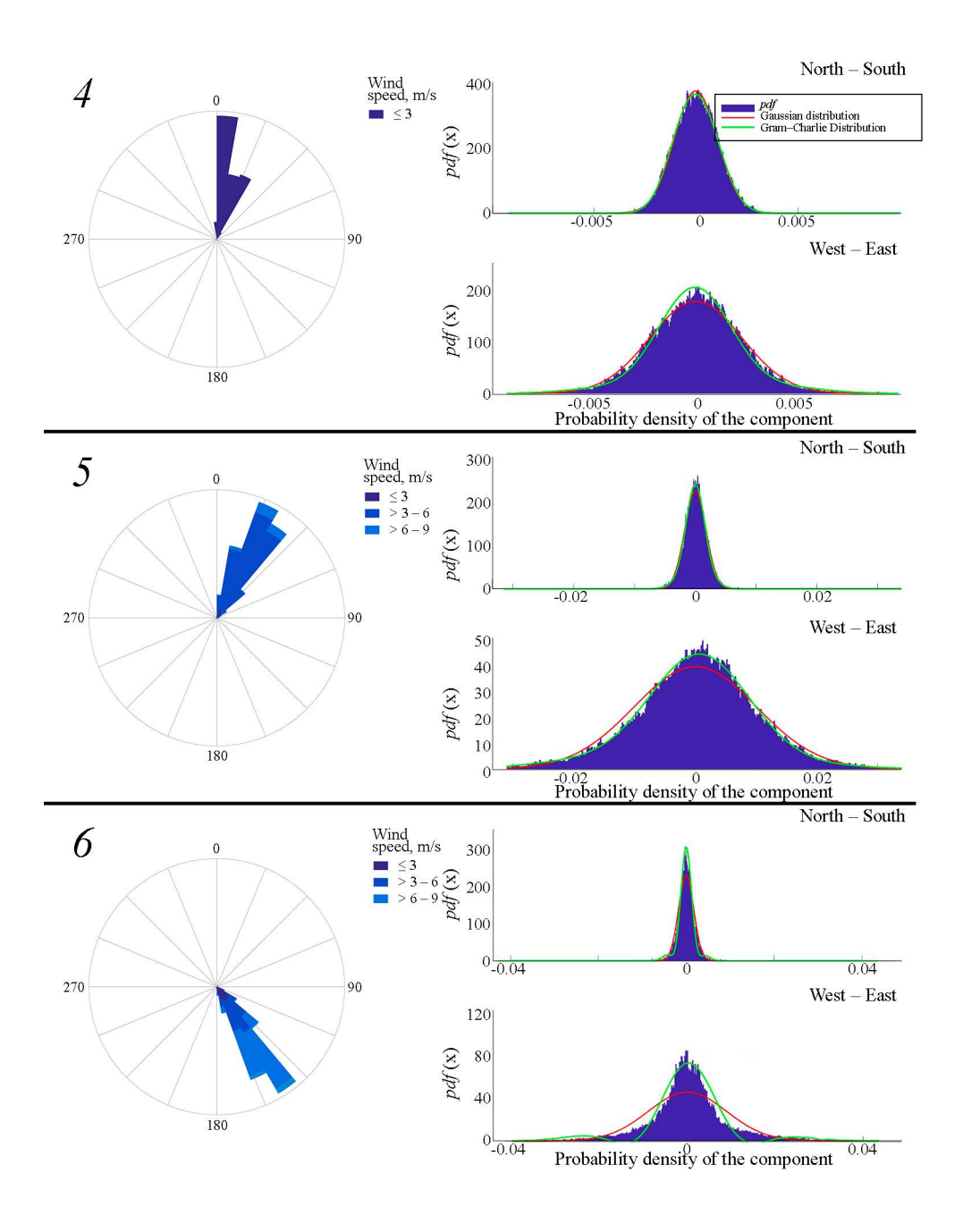


Fig. 7. The same as in Fig. 6, for other dates: 4 - 12.07.2019 during the time period from 20:09:23 to 21:09:23, 5 - 12.07.2019 – from 23:09:24 to 00:09:24, and 6 - 13.07.2019 – from 16:09:30 to 17:09:30

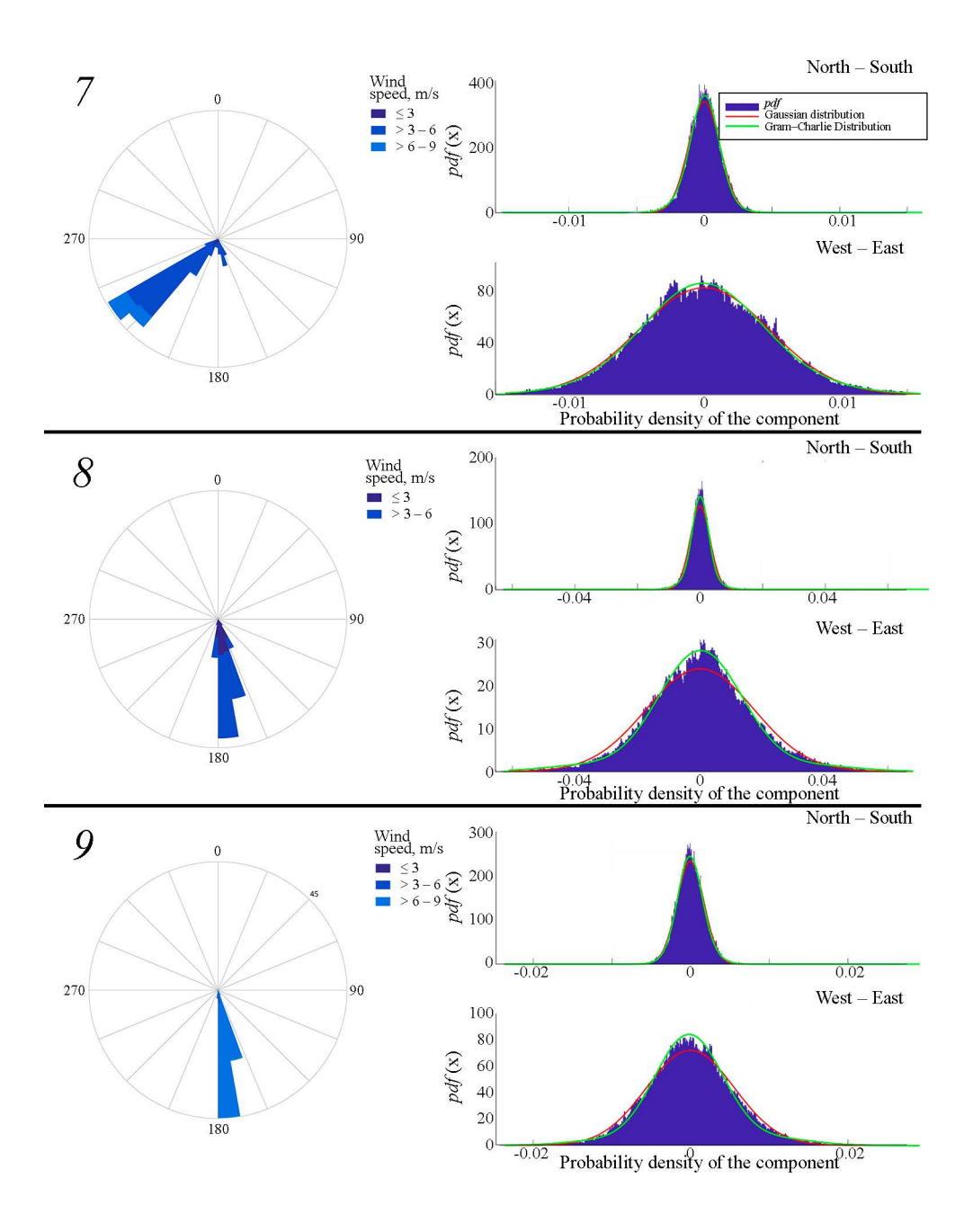


Fig. 8. The same as in Fig. 6, for other dates: 7 - 07.14.2019 during the time period from 16:09:39 to 17:09:39, 8 - 07.15.2019 – from 13:09:46 to 14:09:46, and 9 - 07.17.2019 – from 16:10:04 to 17:10:04

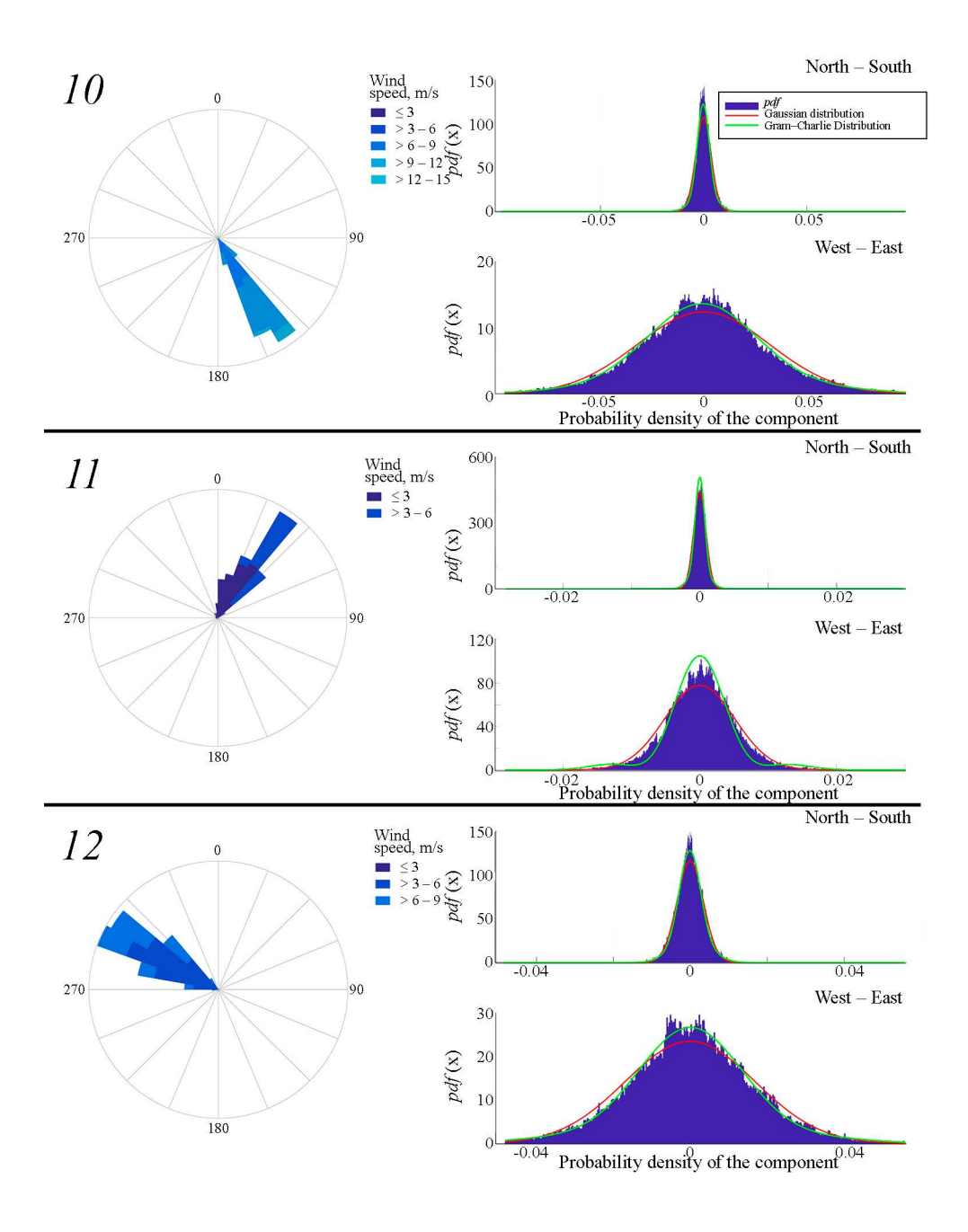


Fig. 9. The same as in Fig. 6, for other dates: 10 - 07.20.2019 during the time period from 16:37:29 to 17:37:29, 11 - 07.24.2019 – from 16:56:39 to 17:56:39, and 12 - 08.02.2019 from 06:10:06 to 07:10:06

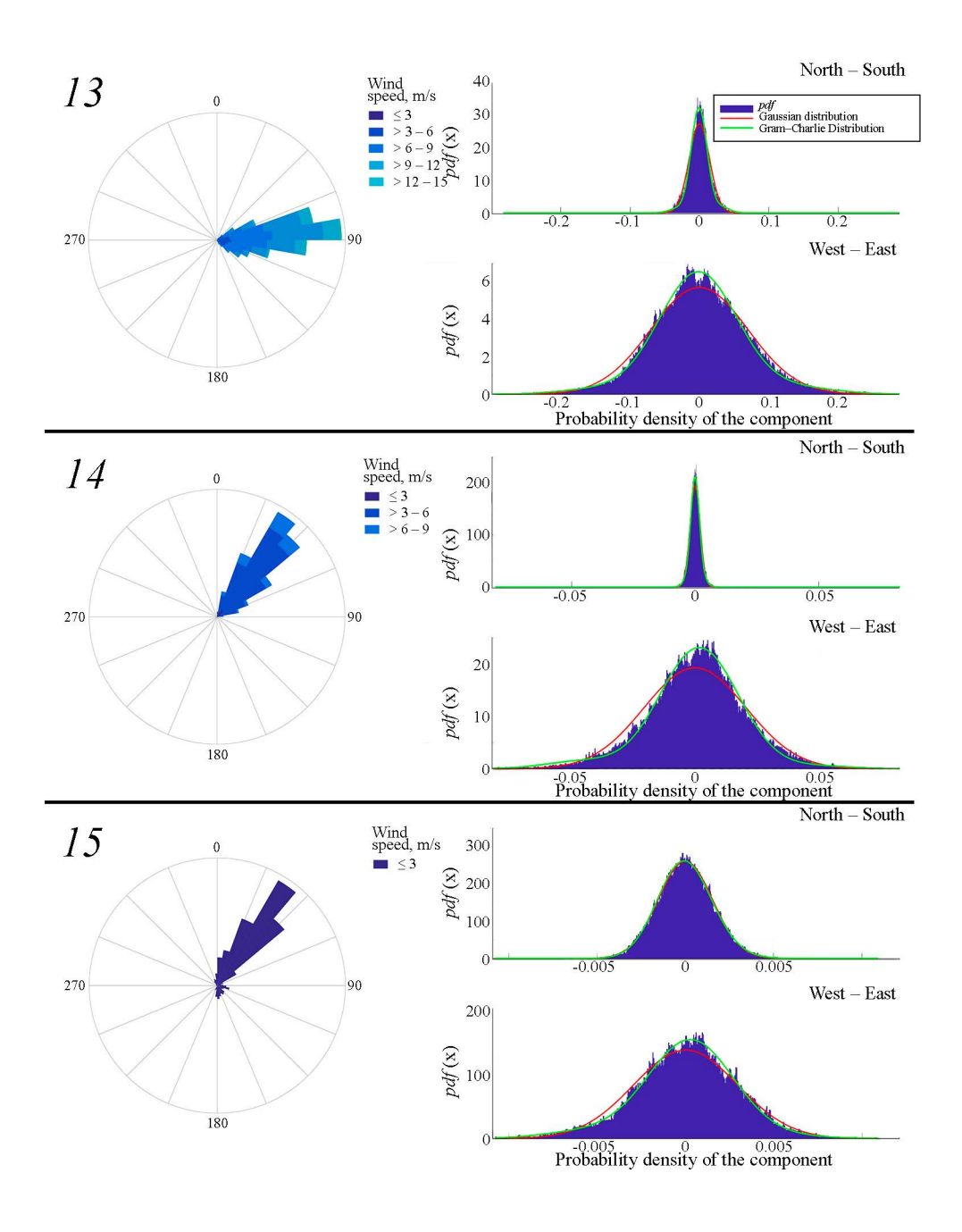


Fig. 10. The same as in Fig. 6, for other dates: 13 - 07.08.2019 during the time period from 16:11:02 to 17:11:02, 14 - 11.08.2019 – from 16:11:39 to 17:11:39, and 15 - 08.06.2020 – from 16:17:16 to 17:17:16

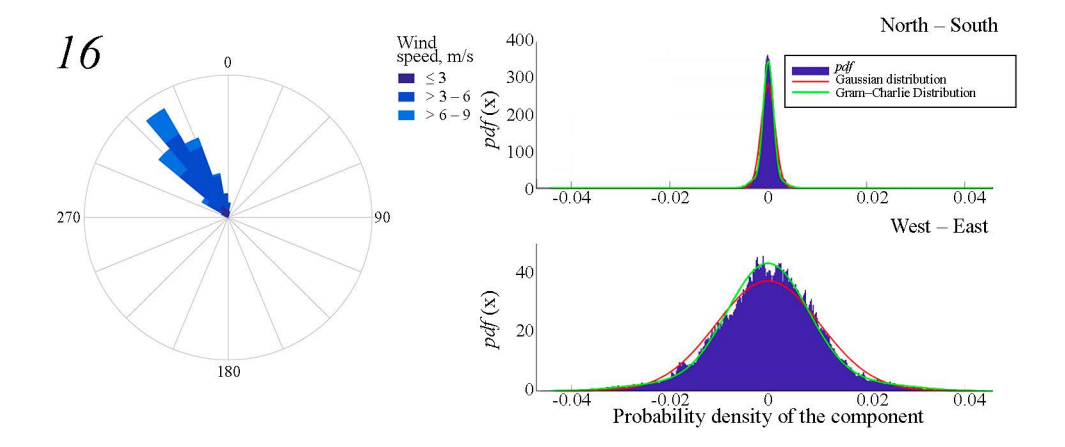
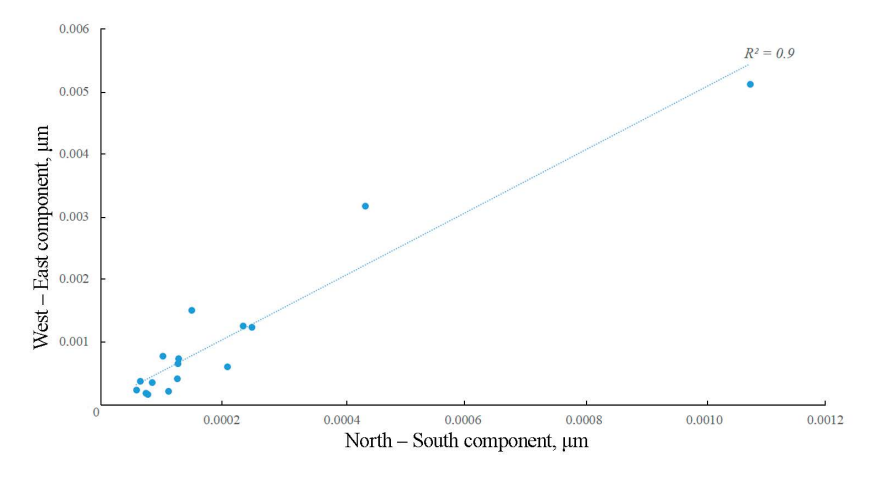


Fig. 11. The same as in Fig. 6, for another date: 16 - 09.19.2020 during the time period from 19:49:27 to 20:49:27

Thus, the conducted analysis showed that the background signal in the frequency range of 0.05–0.5 Hz possesses characteristics close to a normal process. Deviations from normality can be quantitatively assessed using the correction terms in the Gram-Charlier series.

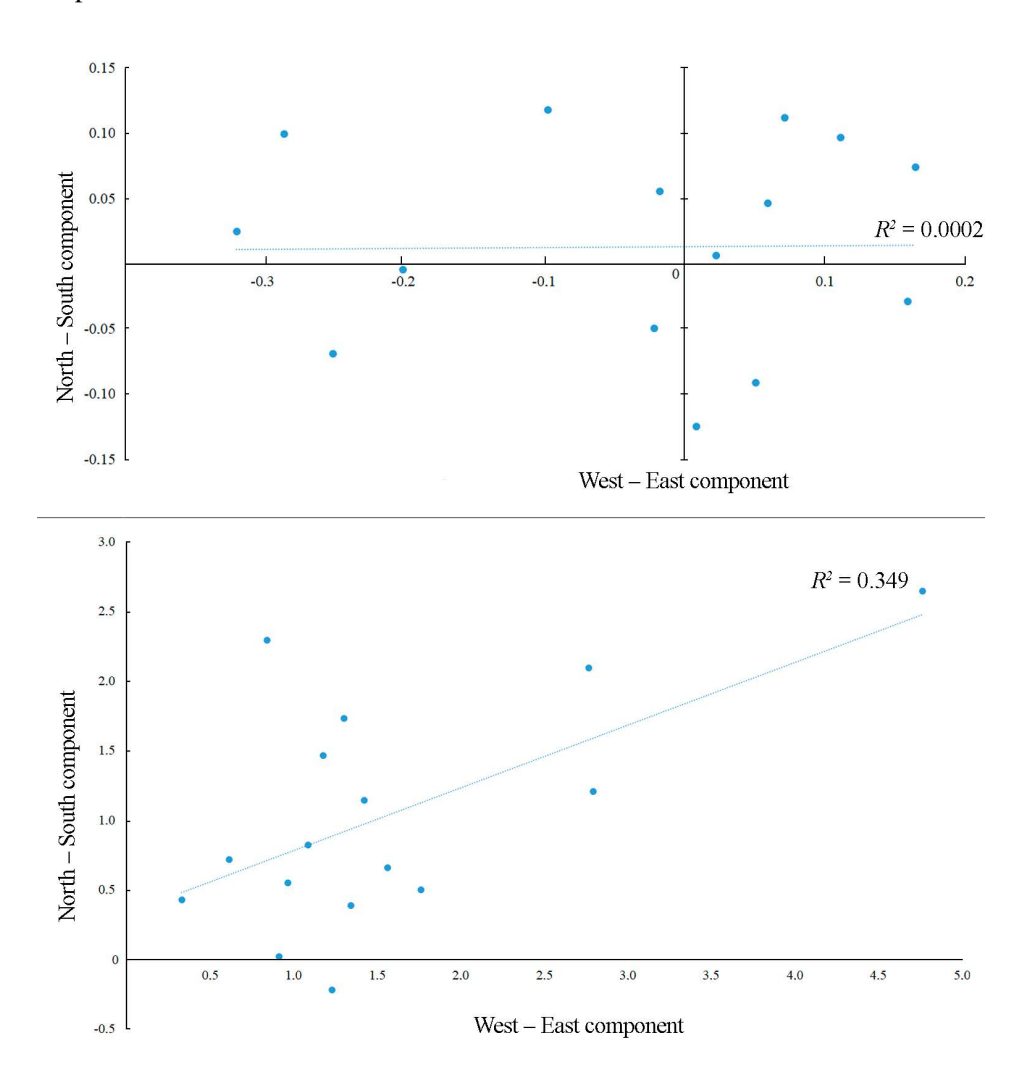
Analysis of the 16 records revealed that for the North – South component, positive skewness (Sk > 0) was observed in 9 cases and negative skewness (Sk < 0) in 7 cases, while for the West – East component, positive skewness was observed in 8 cases and negative skewness in 8 cases. The kurtosis Ku was predominantly positive for both components, with only one kurtosis value for the North – South component being negative. As is known, positive kurtosis values indicate an increased probability of large-amplitude outliers, which are now associated with rogue waves [24]. However, their analysis requires significantly longer record lengths.



 $\label{eq:Fig. 12.} \textbf{East component from the North-South component} \\ \textbf{F i g. 12.} \\ \textbf{Correlation graph of standard deviation of the West-East component from the North-South component} \\ \textbf{South South South Component} \\ \textbf{South South S$

An analysis of the relationships between the components was conducted using the obtained data. Fig. 12 shows a correlation graph of the standard deviation for the two interferometer components, North - South and West - East, featuring a linear trend. The coefficient of determination R^2 , calculated for this approximation, is 0.9. This relationship is likely explained by the manifestation of common physical processes, such as wind loads, sea wave dynamics, atmospheric disturbances, and tidal phenomena, which simultaneously affect both components.

A correlation graph for the skewness and kurtosis coefficients of the two strainmeter components was also constructed (Fig. 13), and the coefficients of determination were calculated: for skewness, 0.0002; for kurtosis, 0.35. Judging from the fragments in Fig. 13, the relationship between these components is practically non-existent, suggesting that they are most likely more sensitive to the specific characteristics of external influences.



 ${f F}$ i ${f g}$. 13. Correlation graph of skewness (top) and kurtosis (bottom) for the West – East and North – South components

Conclusion

A detailed statistical analysis of the background field recorded by laser strainmeters at Shultz Cape in the Sea of Japan during 2019–2020 has been carried out for the first time. The statistical processing of the signal was performed after frequency filtering with a 0.05–0.5 Hz band-pass filter and subsequent signal reconstruction, which removed the trend and high-frequency components. Corresponding signal histograms were constructed for the record fragments (16 in total). It was found that, in general, the distribution is close to normal but is better described by the Gram-Charlier distribution. Analysis of the 16 records showed that for the North – South component, positive skewness was observed in 9 cases and negative in 7 cases, while for the West – East component, positive skewness was observed in 8 cases and negative skewness in 8 cases. The kurtosis was predominantly positive for both components, with only one kurtosis value for the North – South component being negative.

The present study provides the characteristics of the background noise necessary for the subsequent extraction of useful signals against this background.

REFERENCES

- 1. Dolgikh, G.I., Dolgikh, S.G., Chebrov, V.N. and Shevchenko, Yu.V., 2010. Cape of Shults Geophysical Ground. *Vestnik of the Far East Branch of the Russian Academy of Sciences*, (5), pp. 165-169 (in Russian).
- Vinogradov, A.N., Vinogradov, Yu.A. and Malovichko, A.A., 2014. The Applicability of Seismoinfrasound Monitoring for Remote Control of Geodynamic Regime in Oil and Gas Fields of the Kara Sea Shelf and Yamal Peninsula. *Transactions of the Kola Science Centre of RAS*, 4(19), pp. 22-31 (in Russian).
- 3. Kovalev, D.P. and Kovalev, P.D., 2024. Tsunami Waves off the Southeastern Coast of Sakhalin Island Caused by the Eruption of the Hunga–Tonga–Hunga–Ha'apai Volcano on January 15, 2022 According to Observations by Bottom Devices of Waves. *Moscow University Physics Bulletin*, 79(3), pp. 399-407. https://doi.org/10.3103/S0027134924700449
- 4. Tilinina, N., Ivonin, D., Gavrikov, A., Sharmar, V., Gulev, S., Suslov, A., Fadeev, V., Trofimov, B., Bargman, S. [et al.], 2022. Wind Waves in the North Atlantic from Ship Navigational Radar: SeaVision Development and Its Validation with the Spotter Wave Buoy and WaveWatch III. *Earth System Science Data*, 14(8), pp. 3615-3633. https://doi.org/10.5194/essd-14-3615-2022
- Dolgikh, G.I., Batyushin, G.N., Valentin, D.I., Dolgikh, S.G., Kovalev, S.N., Koren', I.A., Ovcharenko, V.V. and Yakovenko, S.V., 2002. Seismoacoustic Hydrophysical Complex for Monitoring the Atmosphere–Hydrosphere–Lithosphere System. *Instruments and Experimental Techniques*, 45(3), pp. 401-403. https://doi.org/10.1023/A:1016031925259
- Dolgikh, G., Dolgikh, S., Chupin, V., Davydov, A. and Mishakov, A., 2023. Remote Seismoacoustic Monitoring of Tropical Cyclones in the Sea of Japan. *Remote Sensing*, 15(6), 1707. https://doi.org/10.3390/rs15061707
- 7. Dolgikh, G. and Dolgikh, S., 2021. Deformation Anomalies Accompanying Tsunami Origination. *Journal of Marine Science and Engineering*, 9(10), 1144. https://doi.org/10.3390/jmse9101144
- 8. Dolgikh, G.I. and Dolgikh, S.G., 2021. Effect of Atmospheric Pressure on the Deformation of the Earth's Crust. *Doklady Earth Sciences*, 500(2), pp. 848-851. https://doi.org/10.1134/S1028334X21100093
- Dolgikh, G.I., Budrin, S.S. and Dolgikh, S.G., 2024. Transformations of Bottom Pressure Variations Generated by Marine Infragravity Waves into Displacements of the Upper Layer of the Earth's Crust: Quantitative Assessment. *Doklady Earth Sciences*, 516(1), pp. 763-767. https://doi.org/10.1134/S1028334X24600841
- 10. Dolgikh, G.I., 2000. The *Investigations of the Wave Fields of the Ocean and Lithosphere by Laser Interference Methods.* Vladivostok: Dalnauka, 160 p. (in Russian).

- Beucler, É., Mocquet, A., Schimmel, M., Chevrot, S., Quillard, O., Vergne, J. and Sylvander, M., 2015. Observation of Deep Water Microseisms in the North Atlantic Ocean Using Tide Modulations. Geophysical Research Letters, 42(2), pp. 316-322. https://doi.org/10.1002/2014GL062347
- Le Pape, F., Craig, D. and Bean, C.J., 2021. How Deep Ocean-Land Coupling Controls the Generation of Secondary Microseism Love Waves. *Nature Communications*, 12(1), 2332. https://doi.org/10.1038/s41467-021-22591-5
- Tanimoto, T. and Anderson, A., 2023. Seismic Noise between 0.003 Hz and 1.0 Hz and Its Classification. *Progress in Earth and Planetary Science*, 10(1), 56. https://doi.org/10.1186/s40645-023-00587-7
- Ardhuin, F., Stutzmann, E., Schimmel, M. and Mangeney, A., 2011. Ocean Wave Sources of Seismic Noise. *Journal of Geophysical Research: Oceans*, 116(C9), C09004. https://doi.org/10.1029/2011JC006952
- 15. Moni, A., Craig, D. and Bean, C.J., 2013. Separation and Location of Microseism Sources. *Geophysical Research Letters*, 40(12), pp. 3118-3122. https://doi.org/10.1002/grl.50566
- Anthony, R.E., Aster, R.C. and McGrath, D., 2017. Links between Atmosphere, Ocean, and Cryosphere from Two Decades of Microseism Observations on the Antarctic Peninsula. *Journal of Geophysical Research: Earth Surface*, 122(1), pp. 153-166. https://doi.org/10.1002/2016JF004098
- Lin, J., Fang, S., Xu, W., Ni, S., Zhang, H. and Yang, T., 2022. Multi-Instrument Observations of Microseisms Generated by Typhoon Kalmaegi (2014) over the Northwestern Pacific. *Earth and Planetary Science Letters*, 594, 117746. https://doi.org/10.1016/j.epsl.2022.117746
- Dolgikh, G.I., Valentin, D.I., Dolgikh, S.G., Kovalev, S.N., Koren, I.A., Ovcharenko, V.V. and Fishchenko, V.K., 2002. Application of Horizontally and Vertically Oriented Strainmeters in Geophysical Studies of Transitional Zones. *Izvestiya, Physics of the Solid Earth*, 38(8), pp. 686-689.
- Dolgikh, G.I., Dolgikh, S.G., Kovalev, S.N., Koren, I.A., Novikova, O.V., Ovcharenko, V.V., Okuntseva, O.P., Shvets, V.A., Chupin, V.A. [et al.], 2004. A Laser Nanobarograph and Its Application to the Study of Pressure-Strain Coupling. *Izvestiya, Physics of the Solid Earth*, 40(8), pp. 683-691.
- Dolgikh, S.G., Budrin, S.S. and Plotnikov, A.A., 2017. Laser Meter for Hydrosphere Pressure Variations with a Mechanical Temperature Compensation System. *Oceanology*, 57(4), pp. 600-604. https://doi.org/10.1134/S000143701704004X
- 21. Dolgikh, G.I. and Privalov, V.E., 2016. *Laser Physics: Basic and Applied Research*. Vladivostok: Reya LLC, 352 p. (in Russian).
- 22. Sayfullin, R.T. and Bochkarev, A.V., 2020. Calculating of Asymmetry and Excess Coefficients for Chromatographic Peaks by Using Chebyshev-Hermite Functions and Gram-Charlier Series. *Vestnik of Samara State Technical University. Technical Sciences Series*, 28(4), pp. 89-105 (in Russian).
- 23. Montgomery, D.C. and Runger, C.G., 2010. *Applied Statistics and Probability for Engineers*. USA: John Wiley and Sons Inc., 784 p.
- Slunyaev, A.V., Pelinovsky, D.E. and Pelinovsky, E.N., 2023. Rogue Waves in the Sea: Observations, Physics, and Mathematics. *Physics-Uspekhi*, 66(2), pp. 148-172. https://doi.org/10.3367/UFNe.2021.08.039038

Submitted 24.04.2025; approved after review 05.06.2025; accepted for publication 11.07.2025.

About the authors:

Grigoriy I. Dolgikh, Academician of RAN, V.I. II'ichev Pacific Oceanological Institute, Far Eastern Branch of Russian Academy of Sciences (43 Baltiyskaya Str., Vladivostok, 690041, Russian Federation), DSc. (Phys.-Math.), Professor, ORCID ID: 0000-0002-2806-3834, Scopus Author ID: 700388822, dolgikh@poi.dvo.ru

Stanislav G. Dolgikh, Head of the Laboratory of Nonlinear Hydrophysics and Natural Disasters, V.I. Il'ichev Pacific Oceanological Institute, Far Eastern Branch of Russian Academy of Sciences

- (43 Baltiyskaya Str., Vladivostok, 690041, Russian Federation), DSc. (Tech.), **ORCID ID: 0000-0001-9828-5929**, **Scopus Author ID: 6604069353**, sdolgikh@poi.dvo.ru
- Mikhail P. Ivanov, Senior Engineer, V.I. Il'ichev Pacific Oceanological Institute, Far Eastern Branch of Russian Academy of Sciences (43 Baltiyskaya Str., Vladivostok, 690041, Russian Federation), ORCID ID: 0000-0003-3178-2634, Scopus Author ID: 58535534600, ivanov.mp@poi.dvo.ru
- Efim N. Pelinovsky, Chief Researcher, A.V. Gaponov-Grekhov Institute of Applied Physics, Russian Academy of Sciences (46 Ul'yanova Str., Nizhny Novgorod, 603155, Russian Federation), DSc. (Phys.-Math.), Professor, ORCID ID: 0000-0002-5092-0302, ResearcherID: I-3670-2013, Scopus Author ID: 7004951110, pelinovsky@gmail.com
- Tatiana G. Talipova, Leading Researcher, A.V. Gaponov-Grekhov Institute of Applied Physics, Russian Academy of Sciences (46 Ul'yanova Str., Nizhny Novgorod, 603155, Russian Federation), DSc. (Phys.-Math.), ORCID ID: 0000-0002-1967-4174, ResearcherID: A-1580-2014, Scopus Author ID: 7004244713, tgtalipova@mail.ru

Contribution of the co-authors:

- **Grigoriy I. Dolgikh** scientific supervision of the research, analysis and interpretation of results, participation in the discussion of the article materials and editing of the manuscript
- **Stanislav G. Dolgikh** conceptualization of the study, formulation of scientific objectives, analysis and interpretation of results, participation in the discussion of the article materials
- **Mikhail P. Ivanov** processing of field data, performing numerical calculations and software implementation, data visualization and presentation, writing the original draft of the manuscript, participation in the discussion of the article materials
- **Efim N. Pelinovsky** conceptualization of the study, formulation of the scientific objectives, overall research supervision, analysis and interpretation of results, participation in the discussion of the article materials
- **Tatiana G. Talipova** development of methodological framework for the research, analysis and interpretation of results, writing the original draft of the manuscript and participation in the discussion of the article materials

The authors have read and approved the final manuscript. The authors declare that they have no conflict of interest.